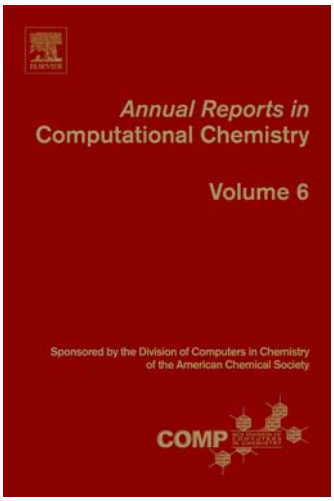

From Darrin M. York, Insights into the Role of Conformational Transitions
and Metal Ion Binding in RNA Catalysis from Molecular Simulations.
In: Ralph A. Wheeler, editor,
Annual Reports in Computational Chemistry (Volume 6).
Elsevier, 2010, p. 169.
ISBN: 978-0-44-453552-8

Section 4
Nanotechnology

Section Editor: Luke E.K. Achenie

Department of Chemical Engineering, Virginia Polytechnic Institute,
Blacksburg, Virginia 24061, USA

CHAPTER 10

Insights into the Role of Conformational Transitions and Metal Ion Binding in RNA Catalysis from Molecular Simulations

Tai-Sung Lee[1,2], **George M. Giambaşu**[1,2], and **Darrin M. York**[2]

Contents

Abstract

We present a summary of recent advances in the application of molecular simulation methods to study the mechanisms of RNA catalysis. The focus of this chapter is on the nature of conformational transitions and metal ion binding on structure and activity. Two RNA enzyme systems are considered: the hammerhead ribozyme and the L1 ligase. The hammerhead ribozyme is a

[1] Biomedical Informatics and Computational Biology, University of Minnesota, Minneapolis, MN, USA

[2] Department of Chemistry, University of Minnesota, Minneapolis, MN, USA

Annual Reports in Computational Chemistry, Volume 6
ISSN: 1574-1400, DOI 10.1016/S1574-1400(10)06010-X

small archetype ribozyme that undergoes a conformational transition into a catalytically active conformation in a step that is concerted with changes in metal ion binding in the active site. The L1 ligase ribozyme is an *in vitro* selected ribozyme that uses a noncanonically base-paired ligation site to catalyze regioselectively and regiospecifically the 5′ to 3′ phosphodiester bond ligation. The L1 ligase presumably undergoes a large-scale conformational change from an inactive to an active form that involves reorientation of one of the stems by around 80 Å, making it a novel catalytic riboswitch. Analysis of the simulation results and comparison with experimental measurements provide important new insight into the conformational and chemical steps of catalysis of the hammerhead and L1 ligase ribozymes.

Keywords: RNA; catalysis; molecular simulation; hammerhead ribozyme; L1 ligase ribozyme; Mg^{2+} ions

1. INTRODUCTION

The original notion that the only function of RNA molecules was as messenger intermediates in the pathway from the genetic code to protein synthesis has undergone a revolution in the past two and a half decades. The role of RNA in cellular function is now known to be considerably more diverse, ranging from regulation of gene expression and signaling pathways to catalyzing important biochemical reactions, including protein synthesis itself [1–7]. These discoveries have transformed our view of RNA as a simple messenger to one more profoundly central in the evolution of life forms, our understanding and appreciation of which is still in its infancy. Ultimately, the elucidation of the mechanisms of RNA catalysis will yield a wealth of new insights that will extend our understanding of biological processes and facilitate the design of new RNA-based technologies [8–10].

Simulations of biological systems at the atomic level could potentially offer access to the most intimate mechanistic details that may aid in the interpretation of experiments and provide predictive insight into relevant drug design or therapeutic efforts [11]. A quantum mechanical (QM) description is ultimately required for reliable study of chemical reactions, including reactions catalyzed by biological macromolecules such as RNA, but at the same time, a high-level fully QM treatment of these systems in molecular simulations is not yet feasible. A practical approach involves the use of so-called "multiscale models" that require only a small, typically localized region of the system to be treated with the most computationally costly QM methods. The term multiscale model here implies the integration of a hierarchy of models that work together to provide a computationally tractable representation of a complex biochemical reaction in a realistic environment. As a specific example, for enzyme systems, one typically treats the reactive chemical events with a sufficiently accurate high-level QM model, the microscopic solvent fluctuations and changes in molecular conformation using molecular mechanical (MM) force field model, and the macroscopic dielectric relaxation using a continuum solvation model. The most simple and

widely applied multiscale model to study enzyme reactions is the use of a combined QM/MM potential [12–16].

RNA catalysis simulations are particularly laden with challenges not apparent for most other biological systems, such as protein enzymes. RNA molecules are highly negatively charged and exhibit strong and often specific interactions with solvent [11,17–19]. This requires special attention to the microscopic *in silico* model that requires consideration of a very large number of solvent molecules and counter and coions to be included. Electrostatic interactions need to be treated rigorously without cutoff, and long simulation times are typically needed to insure that the ion environment is properly equilibrated [20–22]. These issues are further complicated by the fact that RNA molecules bind divalent metal ions that play an important role in folding and, in many instances, also contribute actively to the catalytic chemical steps. The highly charged nature of RNA and its interaction with divalent metal ions and other solvent components makes inclusion of explicit electronic polarization in the molecular models much more important than in typical protein enzyme systems. The chemistry involved in reactions of prototype ribozymes such as cleavage transesterification involves large changes in local charge state and hybridization around phosphorus, exacerbating the need to design QM/MM methods that can reliably model hypervalent states of phosphorus. There is a need to design new models that circumvent the need for "atom-type" parameters to be assigned to the QM system in order to compute QM/MM interactions, as the "atom type" can change as a reaction proceeds. Finally, there is a growing precedent that many ribozyme reactions may involve large changes in conformation and metal ion binding along the reaction coordinate, creating the need to develop extremely fast semiempirical quantum models that can be practically applied in conjunction with long-time simulations to adequately sample relevant configurations and create multidimensional free-energy surfaces along multiple reaction coordinates.

1.1 Hammerhead ribozyme

The hammerhead ribozyme (HHR) [23,24] is an archetype system to study RNA catalysis [25,26]. HHR catalyzes the site-specific attack of an activated 2′OH nucleophile to the adjacent 3′ phosphate, resulting in cleavage of the P–$O_{5'}$ phosphodiester linkage to form a 2′,3′-cyclic phosphate and a 5′ alcohol. A detailed understanding of the structure–function relationships in the HHR [6,24] will ultimately aid in the understanding of other cellular RNA catalysts such as the ribosome. The HHR has gained attention as a potential anti-HIV-1 therapeutic agent [27,28], an inhibitor of *BCR-ABLi1* gene expression [29], an inhibitor of hepatitis-B virus gene expressions [30,31], and a tool in drug design and target discovery for other diseases [9,32]. Very recently, a discontinuous HHR motif has been found embedded in the 3′-untranslated regions of a mammalian messenger RNA, suggesting a possible role in posttranscriptional gene regulation [33]. However, the detailed reaction mechanism of HHR is still elusive despite significant experimental and theoretical work [24,26,34,35].

One aspect of the catalytic mechanism that has perplexed the community involves the specific role of divalent metal ions in catalysis. Specifically, one of the main puzzles involves the apparent inconsistency between the interpretation of thio substitution [36,37] and the mutational [34] experiments with available crystallographic structural information of the minimal hammerhead sequence [38–40]. Biochemical experiments have been interpreted to suggest that a pH-dependent conformational change must precede or be concomitant with the catalytic chemical step, including a possible metal ion bridge between the A9 and scissile phosphates. This is inconsistent with crystallographic data for the minimal hammerhead motif [38–40] ,where A9 and scissile phosphates are found to be ~20 Å apart. Moreover, the function of the 2′OH group of G8 remains unclear from this data [6,24]. Recent crystallographic studies of a full-length HHR have characterized the ground-state active site architecture [41] and its solvent structure [42], including the binding mode of a presumed catalytically active divalent metal ion in the active site. These findings, together with molecular simulation studies [43–46], have reconciled a long-standing controversy between structural and biochemical studies for this system [47].

1.2 L1 Ligase ribozyme

The L1 ligase (L1L) ribozyme, "biology's first enzyme" [48], is an *in vitro* selected ribozyme that uses a noncanonically base-paired ligation site to catalyze regioselectively and regiospecifically the 5′ to 3′ phosphodiester bond ligation, a reaction relevant to origin of life hypotheses that invoke an *RNA World* scenario. No known naturally occurring ribozyme catalyzes this phosphodiester assembly reaction. The concern that RNA might be inherently incapable of catalyzing this reaction was put to rest in 1993 with the first *in vitro* evolution of a ribozyme ligase [49]. Subsequently, several other ribozyme ligases have been produced using *in vitro* selection techniques [50–57], including a small subset that specifically catalyze regiospecific 3′ to 5′ phosphodiester linkages characteristic of all extant RNA and DNA polymerases. L1L [55] is one such example and is unusual in that it uses an intrinsically flexible noncanonically base-paired ligation site [51,58]. In addition to its relevance to the origin of life, the L1L ribozyme, presumably as a fortuitous consequence of *in vitro* selection, functions as an allosteric ribozyme molecular switch [1,59,60]. The L1L can be further engineered to enable derivatives to have their function controlled by small molecules, peptides, or even proteins to create new artificial allosteric ribozymes [55,61–63].

The crystal structure of the L1L ligation product [64] reveals in the same asymmetric unit two crystallographically independent conformations, verifying its postulated intrinsic flexibility. The two conformers differ in the orientation of one of the stems by a movement of its tip by an arc length of around 80 Å [64]. Based on the presence/absence of specific contacts between the ligation site and some distant evolutionarily conserved regions, it was proposed that the conformers represented catalytically active "on" and inactive "off" states [64].

Recently, we have identified the dynamical hinge points of the L1L ribozyme using large-scale molecular dynamics (MD) simulations [65]. We have departed from an analysis of the two crystallized conformers and shown using over 600 ns of MD simulations that the transition between *on* and *off* conformational states can be almost entirely described by changes in only four virtual torsion angles. Virtual torsions are formed along the virtual bonds between $C_{4'}$ and P atoms and have been shown to be able to discriminate between major RNA folds [66,67].

In this chapter, we summarize our recent efforts to unveil the detailed mechanisms of HHR and L1L catalysis using MD simulations and hybrid QM/MM calculations. In the case of the HHR, emphasis is placed on the characterization of metal binding modes at different stages along the reaction coordinate, the role of metal ion interactions on structure and activity, and the origin of mutational effects on catalysis. In the case of the L1L ribozyme, the focus is placed on the identification of dynamical hinge points and the characterization of the conformational transition between catalytically active "on" and inactive "off" states, including induced unfolding resulting from removal of structural divalent metal ions. Together, these studies provide deeper insight into the the role of conformational transitions and metal ion binding in RNA catalysis.

2. MOLECULAR SIMULATIONS OF THE HAMMERHEAD RIBOZYME

In this section, we examine metal ion binding modes in the HHR at various stages of progression along the reaction coordinate. Detailed analysis of these binding modes affords insight into the role of divalent metal ions in catalysis. Moreover, long-time MD simulations allow characterization of the electrostatic environment of the HHR and the ability to recruit cationic charge, that when threshold occupancy is achieved, leads to formation of catalytically active conformations. Further study of HHR mutations provide an atomic level interpretation of the origin of mutational effects.

2.1 Metal binding modes

MD simulations were set up to explore the metal binding modes in the HHR and their relation to structure and catalysis. A recent joint crystallographic/molecular simulation study [42] of the solvent structure of the full-length HHR indicates that, in the reactant state prior to activation of the nucleophile, a Mn^{2+} ion is coordinated to the O_{2P} atom of the A9 phosphate and the N7 atom of G10.1. This binding site is designated as the "C-site." An alternate binding site, where a divalent metal ion bridges A9:O_{2P} and the scissile phosphate (C1.1:O_{2P}) and is designated as the "B-site," has been inferred from thio/rescue effects [36,37] and also predicted from molecular simulations [44,45]. In the absence of divalent metal ions, HHR activity can be recovered by high concentrations of monovalent ions [68–70]. The specific metal ion binding modes at different stages along the HHR reaction coordinate, and their relation to formation of catalytically active

structures, has not yet been determined. Here we report results from a series of MD simulations that aim to provide atomic level insight into these questions.

To explore the divalent and monovalent metal ion binding modes (Figure 1) and their relation to formation of catalytically active, in-line attack conformations in both the neutral reactant and activated precursor (deprotonated 2′OH nucleophile) states, we set up the following series of simulations:

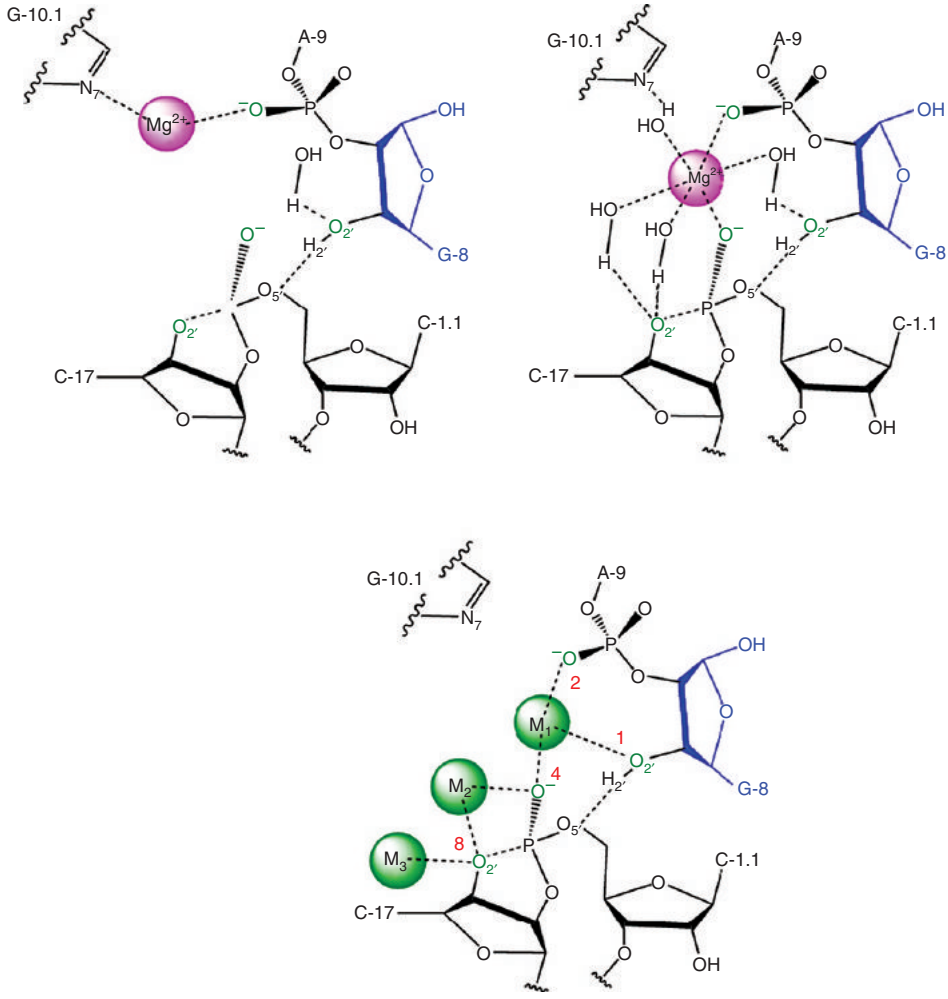

Figure 1 Schematic view of the coordination sites in the hammerhead ribozyme active site. Upper left: The coordination pattern of Mg^{2+} in the "C-site" coordinated to G10.1:N_7 and A9:O_{2P}. Upper right: The coordination pattern of Mg^{2+} in the "B-site" bridging A9:O_{2P} and C1.1:O_{2P} of the scissile phosphate. Lower: Coordination sites for Na^+ in the hammerhead ribozyme active site found in the RT-Na and dRT-Na simulations. Red numbers next to the coordination sites are the scores used to calculate the coordination index (see text). M_1 involves direct binding to A9:O_{2P} and C.1:O_{2P} and indirect binding to G10.1:N_7 through a water molecule. M_2 involves direct binding to C17:$O_{2'}$ and C.1:O_{2P}. M_3 involves direct binding to C17:$O_{2'}$ and is positioned toward the outside of the active site. (For interpretation of the references to colour in this figure legend, the reader is referred to the web version of this book.)

- **RT-C-Mg**, the reactant state with Mg^{2+} at the C-site.
- **RT-B-Mg**, the reactant state with Mg^{2+} at the bridging position.
- **dRT-C-Mg**, the activated precursor with Mg^{2+} at the C-site.
- **dRT-B-Mg**, the activated precursor with Mg^{2+} at the bridging position.
- **RT-Na**, the reactant state in the absence of Mg^{2+} (in the presence of NaCl only).
- **dRT-Na**, the activated precursor in the absence of Mg^{2+} (in the presence of NaCl only).

In the dRT-C-Mg simulation involving the activated precursor with Mg^{2+} initially placed at the C-site, the Mg^{2+} ion quickly (<200 ps) migrates into the B-site position, as observed in a previous simulation study [44], and afterward exhibits nearly identical behavior as if the Mg^{2+} ion was initially placed at the B-site (dRT-B-Mg). Hence, we only extended the dRT-B-Mg simulation to 300 ns and designate it simply as dRT-Mg. All five simulations were carried out to 300 ns in a background of 0.14 M NaCl. The equilibration for each simulation was monitored by the root mean square deviation (RMSD) and was observed to reach a steady state after 30–50 ns. Hence, all analyses were performed over the last 250 ns of trajectories for each simulation.

2.1.1 A bridging Mg^{2+} ion maintains rigid coordination patterns that stabilize in-line attack conformations

In this section, we compare the effect of different Mg^{2+} binding modes in both the neutral reactant and activated (deprotonated 2′OH) precursor states on the active site structure and fluctuations. Table 1 lists the averages of key in-line indexes, the A9/scissile phosphate–phosphate distances, and Mg^{2+} coordination distances for the RT-C-Mg, RT-B-Mg, and dRT-Mg simulations. Figure 1 shows a general schematic view of the active site metal ion coordination from the simulations. The distances and standard deviations indicate that the Mg^{2+} ion retains rigid coordination with the phosphate oxygens over the course of the simulation, being directly coordinated to A9:O_{2P} in all simulations. In the RT-C-Mg simulation, the Mg^{2+} ion coordinates G10.1:N_7 indirectly through one of four inner-sphere water molecules. However, this coordination pattern is not highly

Table 1 Characterization of the Mg^{2+} coordination in the active site

	R	θ	O–O	A9:O_{2P}	C1.1:O_{2P}	C17:$O_{2'}$	G8:$O_{2?}$	G10:N_7
RT-C-Mg	4.01(34)	126.5(119)	4.14(49)	2.01(4)	4.40(30)	6.04(90)	5.76(46)	4.19(31)
RT-B-Mg	3.28(12)	151.2(79)	2.95(13)	2.02(5)	2.04(5)	4.25(24)	4.57(30)	4.38(25)
dRT-Mg	3.64(17)	155.0(80)	2.94(13)	2.01(4)	2.03(5)	3.76(17)	4.62(62)	5.05(26)

Analysis was performed over the last 250 ns (10 ps sampling frequency). Distances and angles (Figure 1) are in angstrom and degrees, respectively. Standard deviations (SDs) are listed in parenthesis divided by the decimal precision of the average (e.g., if the average is reported to two digits of decimal precision, the SD is divided by 0.01). R is the in-line attack distance (C17:$O_{2'}$ to C1.1:P), and is the in-line attack angle (between C17:$O_{2'}$, C1.1:P, and C1.1:$O_{5'}$). *O–O* is the distance between A9:O_{2P} and C1.1:O_{2P}, and other distances are between the Mg^{2+} and the indicated ligand site.

conducive to formation of an in-line attack conformation. The RT-B-Mg simulation, on the other hand, shows a more rigid Mg^{2+} coordination with both the A9 and scissile phosphate oxygens and sustains a considerable population of in-line attack conformations. These results suggest that the coordination pattern found in the RT-B-Mg simulation is able to stabilize in-line attack conformations more readily than Mg^{2+} binding at the C-site as in the RT-C-Mg simulation. The dRT-Mg simulation is similar to the RT-B-Mg simulation with regard to exhibiting rigid coordination with the A9 and scissile phosphate oxygens and stabilization of in-line attack conformations.

With the Mg^{2+} ion at the bridging position (RT-B-Mg and dRT-Mg simulations), there is considerably reduced interaction with G10.1:N_7, which are compensated by interactions with the C17:$O_{2'}$ that occur through two water molecules in the inner sphere of the Mg^{2+} ion. This interaction is most pronounced in the dRT-Mg simulation where the C17:$O_{2'}$ is deprotonated. In the ground-state reactant simulations with Mg^{2+} (RT-C-Mg and RT-B-Mg), no Na^+ ions were observed to infiltrate the active site. In the activated precursor simulation, dRT-Mg, a single Na^+ ion, was observed to be bound at high occupancy to the deprotonated C17:$O_{2'}$ in a manner similar to the M_3 position in Figure 1.

2.1.2 Specific Na^+ binding patterns are correlated with formation of in-line attack conformations

In this section, we explore the monovalent metal ion binding modes that are correlated with formation of catalytically active in-line attack conformations. For the simulations with no Mg^{2+} ions (RT-Na and dRT-Na) in the active site, binding of the Na^+ ions to the coordination sites exhibits larger variation, and exchange events occur giving rise to a fairly broad array of coordination patterns. In order to characterize the distribution and frequency of this array of coordination patterns, a binary-coded coordination index is used (Figure 1). This index is defined as follows: when a Na^+ is within a cutoff distance (3.0 Å) to a ligand, it is classified as bound to the ligand and assigned a unique coordination score for binding to that particular ligand. The coordination scores for the four possible coordination sites (ligands) are 1 for G8:$O_{2'}$, 2 for A9:O_{2P}, 4 for C1.1:O_{2P}, and 8 for C17:$O_{2'}$. The coordination index of an ion is the sum of all coordination scores from its bound sites. In this way, the coordination pattern of a Na^+ can be uniquely represented by a single number. For example, an index of 12 means that a Na^+ directly coordinates to both C1.1:O_{2P} and C17:$O_{2'}$ simultaneously (4 + 8 = 12). Through this coordination index, the coordination patterns of Na^+ ions in the active site can be traced as a time series over the course of the simulation as shown in Figure 2. Distinct colors are also used to distinguish individual Na^+ ions present in the active site such that transitions between coordination patterns (indexes) can be monitored.

Figure 2 shows that in the RT-Na simulation, two Na^+ ions (colored as red and green) are present in the active site and, most of time, they both have a

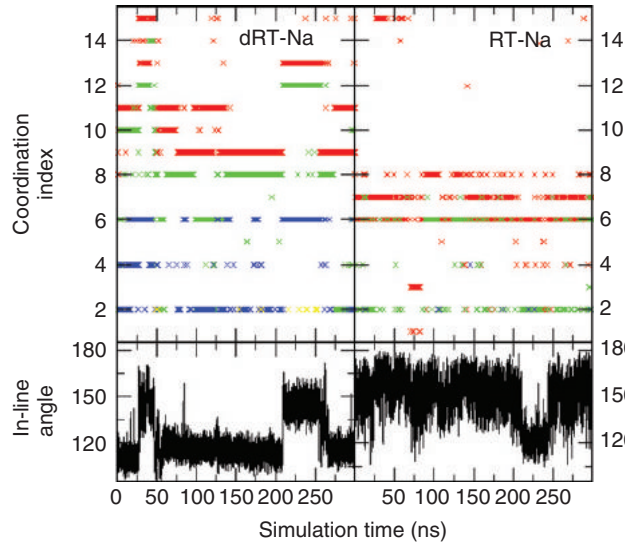

Figure 2 Plot of the in-line attack angle ($O_{2'}$–$O_{5'}$) in degrees and the coordination index of Na^+ ions for the dRT-Na (left) and RT-Na (right) simulations. The coordination index is defined as follows: when a Na^+ ion has a distance less than a 3.0 Å cutoff value to a ligand, it is defined as bound to that ligand for indexing purposes. When an ion is bound, the scores for the four possible coordination sites are 1 for G8:$O_{2'}$, 2 for A9:O_{2P}, 4 for C1.1:O_{2P}, and 8 for C17:$O_{2'}$. The coordination index of a single Na^+ ion is the sum of all scores from its bound sites. Individual Na^+ ions are tracked using different colors (red, green, blue, and yellow). Data obtained from the last 250 ns are shown in steps of 500 ps. (For interpretation of the references to colour in this figure legend, the reader is referred to the web version of this book.)

coordination index of 6, indicating binding to both A9:O_{2P} and C1.1:O_{2P} at the same time (2 + 4 = 6, refer to Figure 1). Hence, two Na^+ ions collectively act like a single bridging Mg^{2+} ion to hold the negatively charged A9 and scissile phosphates together to maintain an in-line conformation. During the period from ~210 to 240 ns, only one Na^+ ion (red) with coordination index of 6 is present in the active site. During this period, the in-line angle drops suddenly from around 155° to 120°. In those periods, the in-line conformation is no longer held.

In the dRT-Na simulation, the in-line angle is less well preserved than in the dRT-Mg simulation. This is consistent with the lower activity of the ribozyme in the absence of Mg^{2+}. Nonetheless, there are several periods (e.g., 25–50 ns and 210–270 ns) where an in-line conformation is visited, and again we observe a high correlation between the Na^+ ion coordination index and the in-line conformation. When less than three Na^+ ions bind to the active site ligands, the in-line conformation is no longer held, which happens during most of the simulation. The in-line attack angle comes to a ready-to-react value (> 150°) when three Na^+ ions bind simultaneously to different ligand sites.

Figure 3 illustrates the different Na^+ binding patterns for cluster A, (defined in Table 2, in-line conformation, lower panels) and cluster B (not in-line conformation, upper panels) from the dRT-Na simulation. The in-line cluster A clearly exhibits three Na^+ bridges that involve C17:$O_{2'}$/C1.1:O_{2P}, C1.1:O_{2P}/G8:$O_{2'}$, and

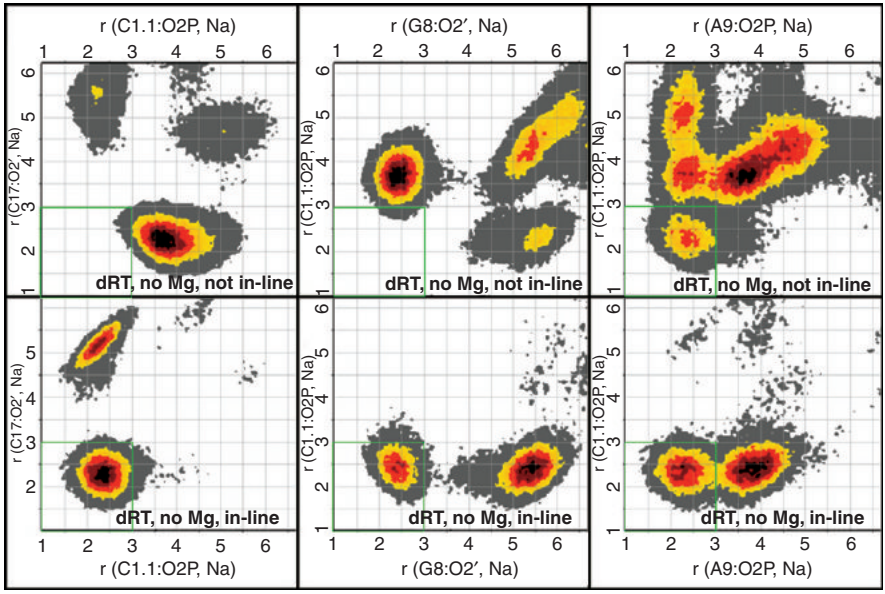

Figure 3 Two-dimensional radial distribution function of Na^+ ions in the active site for the activated precursor simulation without Mg^{2+} present in the active site (dRT-Na). The lower panels show results for cluster A that contains population members that are in active in-line conformations, and the upper panels show results for cluster B that are not in-line (see Table 2). The axes are the distances (in Å) to different metal coordination sites. The green lines indicate the regions where Na^+ ions have distances less than 3.0 Å to both sites indicated by the axes. (For interpretation of the references to colour in this figure legend, the reader is referred to the web version of this book.)

C1.1:O_{2P}/A9:O_{2P}. On the other hand, for cluster B, the first two of these bridges are absent with the third one being significantly less pronounced.

The above analysis suggests that the compensation of the negative charges of these three coordination sites, as well as the bridging binding patterns of Na^+ to bring them together, is necessary to keep the in-line conformation in the deprotonated activated precursor state, although the binding patterns are not as rigid as those of Mg^{2+}.

2.1.3 HHR folds to form a cation recruiting pocket in the active site

In this section, we examine the preferential occupation of cations in the HHR active site. The 3D density contour maps for the Na^+ ion distribution determined over the last 250 ns of simulation (Figure 4) show that the average Na^+ ion density at a medium contour level (left panels, Figure 4) is located near the RNA's phosphate backbone, whereas at high contour level (right panels, Figure 4) the highest probability Na^+ occupation sites were all concentrated in the active site for both the reactant and activated precursor. No explicit Na^+ ions were initially placed in the active site, and Na^+ ion exchange events were observed to occur.

These results suggest that the HHR folds to form a strong local electronegative pocket that attracts cations from solution (e.g., either Mg^{2+}, if present,

Table 2 Coordination patterns of Mg^{2+} and Na^{+} ions in active site

	Cluster	Percentage	*R*	θ	$\langle N_{Mg^{2+}} \rangle$	$\langle CN_{Mg^{2+}} \rangle$	$\langle NB_{Mg^{2+}} \rangle$	$\langle N_{Na^{+}} \rangle$	$\langle CN_{Na^{+}} \rangle$	$\langle NB_{Na^{+}} \rangle$
RT-C-Mg	A	20.78%	3.30	144.05	1.00	1.00	0.00	0.05	1.00	0.00
	B	79.22%	4.13	122.66	1.00	1.00	0.00	0.03	1.00	0.00
RT-B-Mg	A	99.54%	3.27	151.10	1.00	2.00	1.00	0.00	1.00	0.00
	B	0.46%	4.00	129.76	1.00	2.00	1.00	0.09	1.00	0.00
RT-Na	A	86.72%	3.23	152.91	–	–	–	1.15	1.99	0.88
	B	13.28%	4.12	122.82	–	–	–	1.38	1.54	0.66
dRT-Mg	A	100.00%	3.64	154.89	1.00	2.00	1.00	0.97	1.01	0.01
dRT-Na	A	23.99%	3.50	144.72	–	–	–	2.96	2.29	2.68
	B	76.01%	4.30	115.16	–	–	–	2.46	1.69	1.36

Distances and angles (Figure 1) are in angstrom and degrees, respectively. The average values, denoted as $\langle \ldots \rangle$, are obtained by averaging over all snapshots in the cluster. *R* is the in-line attack distance (C17:$O_{2'}$ to C1.1:P). θ is the in-line attack angle (between C17:$O_{2'}$, C1.1:P, and C1.1:$O_{5'}$). *N* is the number of ions with at least one coordination to any one of the four coordination sites. *CN* is the total coordination number of all ions with at least one coordination to any one of the four coordination sites. *NB* is the number of ions which coordinate to at least two of the four coordination sites.

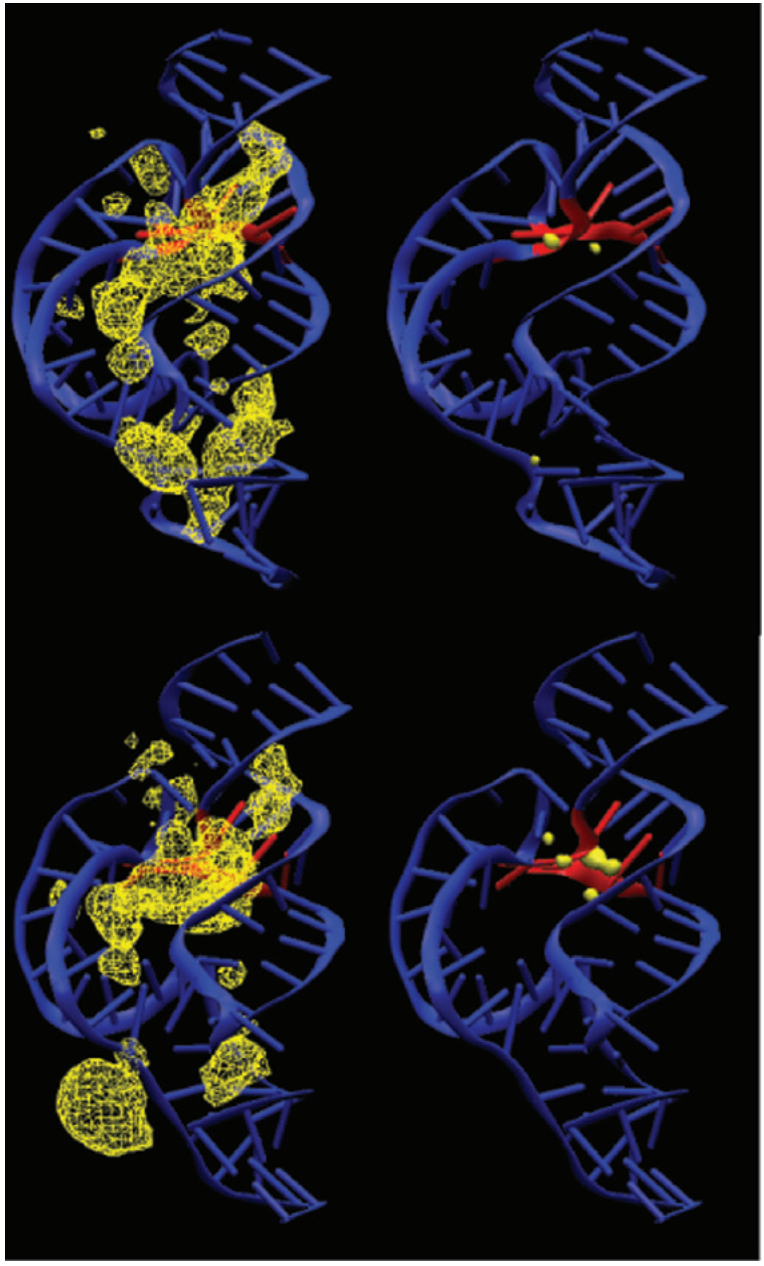

Figure 4 The 3D density contour maps (yellow) of Na^+ ion distributions derived from the RT-Na (upper panels) and dRT-Na simulations (low panels) at different isodensity contour levels (left panels: 0.1; right panels: 1.0). The hammerhead ribozyme is shown in blue with the active site highlighted red. The figure shows that, although the Na^+ ions distribute around the RNA phosphate backbone (left panels), the hammerhead ribozyme folds to form a local electronegative recruiting pocket that attracts a highly condensed distribution of the Na^+ ions (left panels) both in the reactant state and in the deprotonated activated precursor-state (deprotonated C17:$O_{2'}$) simulations. (For interpretation of the references to colour in this figure legend, the reader is referred to the web version of this book.)

or Na^+). As discussed previously, threshold occupancy of cationic charge and specific metal ion binding patterns (in particular, bridging coordination of the A9 and scissile phosphates) stabilize the active site and facilitate formation of in-line attack conformations. As analyzed by NMR, a similar case has been observed in the tetraloop–receptor complex, where the divalent ions were experimentally found to be located at strong electronegative positions formed by the RNA fold [71].

Together with the known divalent metal ion binding at the C-site, these results provoke the speculation that perhaps the active sites of some ribozymes such as the HHR have evolved to form electrostatic cation binding pockets that facilitate catalysis. In the case of the HHR, this speculation is further supported by the simulated correlation of cation binding mode with formation of active conformations discussed in detail in the previous sections.

2.2 Simulations along the reaction coordinate

In the previous section, we showed that the active site Mg^{2+} ion prefers to occupy the C-site and B-site in the reactant state and in the deprotonated active precursor, respectively. Starting with these two possible sites, simulations have been performed for transition state (TS) mimics to explore the possible roles of the Mg^{2+} ion in the chemical reaction step, including four MD simulations of the reactant state in protonated (RT) or activated/deprotonated (dRT) form, two simulations of the early TS (ETS) and two simulations of the late TS (LTS) with the Mg^{2+} ion initially placed at C-site (c-) or B-site (b-), and finally two additional QM/MM simulations of the ETS and LTS.

2.2.1 Molecular dynamics studies of transition state mimics

In the TS mimic simulations with Mg^{2+} initially placed at the C-site, in both ETS and LTS (c-ETS and c-LTS), the Mg^{2+} ion migrates from the C-site to the bridging position in less than 0.5 ns and remains at the B-site for the remainder of the simulation, as postulated previously [45]. This migration is likely facilitated by deprotonation of the 2′OH of C17 (the nucleophile) and the accumulation of negative charge that is formed in moving toward the TS. These results are consistent with thio/rescue effect experiments indicating that both the A9 phosphate oxygens and the pro-R_P scissile phosphate oxygen exhibit a stereospecific kinetic thio effect in the presence of Mg^{2+} that can be rescued by Cd^{2+} ions [37]. Since both c-ETS and c-LTS resulted in the migration of Mg^{2+} to the B-site, we will focus only on the ETS and LTS mimic simulations with Mg^{2+} initially placed at the B-site and labeled here b-ETS and b-LTS respectively.

In b-ETS and b-LTS simulations, the distance between the A9 and scissile phosphates keeps around 4 Å and the Mg^{2+} coordination between the C1.1 and A9 phosphate oxygens keeps an axial–axial position along the whole simulations (Table 3). The distance between the A9 and scissile phosphates in the crystallographic structure is around 4.3 Å, which is well suited for Mg^{2+}-bridging coordination [72]. A similar situation is found in the

Table 3 Comparison of crystallographic and simulation data for selected heavy-atom distances (Å) in the hammerhead active site

	X-ray		Simulation		
	2GOZ	2OEU	b-RT	b-ETS	b-LTS
C1.1:O_{2P}…A9:O_{2P}	4.33	4.28	3.36(49)	4.00(60)	4.01(70)
Mg…G8:$O_{2'}$	3.04	3.14	3.97(102)	2.24(13)	3.21(23)
Mg…C1.1:$O_{5'}$	3.84	4.01	4.22(21)	3.68(35)	2.09(50)
G8:$O_{2'}$…C1.1:$O_{5'}$	3.19	3.51	4.29(77)	4.41(65)	2.91(17)
C17:$O_{2'}$…C1.1:P	3.18	3.30	3.61(23)	1.89(12)	1.76(40)
G12:N1…C17:$O_{2'}$	3.54	3.26	3.02(27)	3.14(28)	2.97(13)
A9:N6…G12:N3	2.63	3.22	3.27(58)	3.15(21)	3.17(21)
A9:N6…G12:$O_{2'}$	3.21	2.98	3.36(86)	3.01(18)	2.99(16)
A9:N7…G12:N2	2.90	2.90	3.42(93)	3.85(44)	3.66(33)

Results are from simulations with Mg^{2+} initially placed at the bridging position for the reactant state (b-RT), the early transition state (b-ETS) mimic, and the late transition state (b-LTS) mimic. Average values are shown with standard deviations in the parenthesis (divided by the decimal precision). X-ray structures used for comparison include the full-length hammerhead RNA crystallographic structure at 2.2 Å resolution (2GOZ) [41] that was also used in this chapter as the starting structure, and the 2.0 Å resolution structure with resolved Mn^{2+} sites and solvent (2OEU) [42].

deprotonated reactant-state simulation presented in the previous section that discusses the Mg^{2+} binding modes.

Specifically, in the ETS mimic simulations, where the nucleophilic $O_{2'}$ and leaving group $O_{5'}$ are equidistant from the phosphorus, the Mg^{2+} ion becomes directly coordinated to the 2′OH of G8 and is positioned closer to the leaving group $O_{5'}$. Both ETS mimic simulations with Mg^{2+} initially placed at the bridging position and the C-site position showed very similar results. The coordination of the Mg^{2+} ion in the ETS mimic simulations is consistent with a role of shifting the pK_a of the 2′OH in G8 so as to act as a general acid.

In the LTS mimic simulations, both with Mg^{2+} initially placed at the bridging and the C-site positions, a transition occurs whereby the Mg^{2+} coordination with the 2′OH of G8 is replaced by direct coordination with the leaving group $O_{5'}$. In this way, the Mg^{2+} may provide electrostatic stabilization of the accumulating charge of the leaving group (i.e., a Lewis acid catalyst) [35]. At the same time, the 2′OH of G8 forms a hydrogen bond with the leaving group $O_{5'}$ and is positioned to act as a general acid catalyst.

2.2.2 Metal-assisted proton transfer in the general acid step

The classical MD simulations in the previous section suggest that in the ETS, the Mg^{2+} ion is positioned to shift the pK_a of the 2′OH of G8 to act as a general acid, and in the LTS, the Mg^{2+} ion can act as a Lewis acid catalyst to stabilize the leaving group and is poised to assist proton transfer from the 2′OH of G8. The possible roles inferred from purely classical MD simulations are supported by

the QM/MM results as a similar binding pattern is observed. The Mg^{2+} ion is bonded to G8:$O_{2'}$ in the ETS mimic and switches to C1.1:$O_{5'}$ of the leaving group in the LTS mimic. In the LTS mimic, the G8:$HO_{2''}$ is strongly hydrogen bonded to C1.1:$O_{5'}$.

In fact, the proton transfer from G8:$O_{2'}$ to C1.1:$O_{5'}$ occurs spontaneously within 1 ns in the QM/MM simulation of LTS mimics. At the start of the simulation, C1.1:$O_{5'}$ is tightly bound to Mg^{2+}, while G8:$O_{2'}$ is around 3 Å away from Mg^{2+}. As the simulation proceeds, G8:$O_{2'}$ moves closer to Mg^{2+} and eventually binds to Mg^{2+} as it gives up its proton to C1.1:$O_{5'}$. After being protonated, the binding between C1.1:$O_{5'}$ and Mg^{2+} becomes weaker and their direct coordination becomes broken. This QM/MM simulation confirms that Mg^{2+} enhances the acidity of G8:$O_{2'}$ and facilitates proton transfer to the leaving group.

2.3 Simulations of mutations of key residues

In this section, we report MD simulations of the native and mutated full-length HHRs in the reactant state and in an activated precursor state (C17:$O_{2'}$ deprotonated). Each simulation has a production trajectory of 60 ns. There exists a wealth of experimental mutational effect data, and simulations of key mutations can offer a detailed rationalization of these effects in terms of structure and dynamics, forge a closer connection between theory and experiment, and provide deeper insight into mechanism. Simulations were performed with the C3U, G8A, and G8I single mutants, and a C3U/G8A double mutant that exhibits an experimental rescue effect [73].

Simulation-derived key active site structural parameters are provided in Table 4, and representative hydrogen-bond base pairing at the C3–G8 positions are shown in Figure 5. In addition, a set of control simulations were performed on a benign U7C mutation, and the wild-type simulation with the active site Mg^{2+} ion removed. An implicit assumption herein is that the mutated sequences fold to a native-like structure.

Mg^{2+} can migrate to a bridging position in the activated precursor. In all reactant-state simulations, the Mg^{2+} stays near A9:O_{2P} and G10.1:N_7. In all activated precursor state (deprotonated C17:$O_{2'}$) simulations, after few hundred picoseconds, the Mg^{2+} migrates into a bridging position between A9:O_{2P} and C1.1:O_{2P}, and reduces the distance (d_0 in Table 4) by 1 Å relative to the reactant-state simulations. The C17:$O_{2'}$ has significant in-line fitness for nucleophilic attack on C1.1:P. In all simulations except G8A, the G8:$O_{2'}$ is hydrogen bonded to the leaving group C1.1:$O_{5'}$ and positioned to act as the general acid.

C3U mutation disrupts the active site in the reactant. The C3U mutation reduces the catalytic rate by a factor ~310^{-4} [76]. The C3U mutation disrupts the normal Watson–Crick hydrogen bonding with G8 (Figure 5), causing a base shift that disrupts the active site structure in the reactant state. The distance between the A9 and scissile phosphates increases more than 3.5 Å and breaks key hydrogen bonds between the $O_{2'}$ nucleophiles of C17 and N_1 of G12 (the implicated general base), and between the $O_{5'}$ leaving groups of C1.1 and H_2 of G8 (the implicated general

Table 4 Characterization of the active site structure and fluctuations. Analysis was performed over the last 25 ns (10 ps sampling)

	WT	NoMg	U7C	C3U	G8A	C3U/G8A	G8I
d_0	3.98(40)	3.40(30)	4.06(40)	**7.80(66)**	4.22(34)	3.94(39)	4.27(59)
r_{Nu}	3.98(34)	3.18(12)	4.08(17)	**4.16(14)**	3.2(10)	3.59(48)	3.77(44)
θ_{inl}	128.2(116)	159.6(82)	121.7(65)	127.1(67)	156.0(70)	141.3(169)	131.6(152)
F[a]	0.29(15)	0.72(10)	0.24(6)	0.23(4)	0.68(9)	0.49(23)	0.37(20)
r_1	2.00(17)	2.12(23)	1.98(17)	–	–	–	–
θ_1	162.9(89)	163.4(89)	163.7(85)	–	–	–	–
r_2	2.01(10)	2.04(13)	2.00(10)	2.25(26)	–	2.04(21)	2.01(14)
θ_2	160.9(90)	162.7(83)	161.0(88)	157.0(127)	–	160.7(104)	162.0(88)
r_3	1.88(12)	1.86(11)	1.89(12)	1.90(13)	2.13(39)	2.06(22)	1.98(19)
θ_3	164.2(85)	161.8(98)	164.8(81)	163.1(88)	149.4(151)	161.2(101)	163.6(90)
r_{NN}[b]	2.97(9)	3.01(12)	2.96(9)	**3.61(21)**	**5.33(66)**	3.00(19)	2.98(13)
r_{HB}	2.10(26)	1.96(14)	2.11(27)	**3.51(66)**	2.01(16)	2.38(46)	2.05(26)
θ_{HB}	152.1(138)	154.9(90)	150.7(136)	**121.2(155)**	164.2(85)	147.1(181)	155.6(124)
r_{HA}	2.83(44)	4.61(94)	2.92(55)	**7.82(58)**	2.97(33)	3.27(64)	2.83(86)
θ_{HA}	118.2(168)	90.7(506)	112.6(205)	**45.2(164)**	119.3(150)	130.6(198)	118.5(344)
%[c]	24.4	0.0	22.4	**0.0**	31.2	13.2	38.4
	d-WT[d]	d-NoMg	d-U7C	d-C3U	d-G8A	d-C3U/G8A	d-G8I
d_0	2.96(12)	3.51(76)	2.94(12)	2.94(13)	2.95(12)	2.93(12)	2.93(13)
r_{Nu}	3.54(17)	3.85(44)	3.59(15)	3.67(16)	3.80(18)	3.62(16)	3.58(18)
θ_{inl}	158.6(78)	**139.2(185)**	156.2(69)	154.2(74)	146.6(88)	155.5(73)	156.6(73)
F[a]	0.52(10)	**0.34(18)**	0.49(8)	0.45(8)	0.38(8)	0.48(8)	0.50(9)
r_1	1.90(14)	1.94(15)	2.02(17)	–	–	–	–
θ_1	160.1(103)	162.6(91)	163.7(85)	–	–	–	–
r_2	1.98(11)	1.99(10)	2.00(10)	1.92(15)	–	2.08(17)	1.95(11)
θ_2	163.1(84)	161.6(85)	162.6(86)	160.5(109)	–	160.8(101)	164.3(82)
r_3	2.02(20)	1.91(13)	1.88(11)	1.93(15)	**2.82(44)**	1.96(17)	2.11(22)

(*Continued*)

θ_3	163.3(93)	164.7(83)	163.8(85)	161.9(94)	**106.9(116)**	160.3(105)	163.2(95)
r_{NN}[b]	2.96(10)	2.96(9)	2.97(9)	**3.75(20)**	**6.58(46)**	3.04(15)	2.93(11)
r_{HB}	2.16(55)	1.97(18)	1.95(15)	1.94(14)	1.89(12)	1.95(14)	1.99(16)
θ_{HB}	152.0(151)	154.9(90)	155.7(96)	158.5(90)	155.5(93)	156.0(99)	
r_{HA}	2.82(95)	**3.28(130)**	2.31(51)	2.99(99)	**4.10(63)**	2.61(91)	2.47(52)
θ_{HA}	126(398)	**92.4(559)**	143.4(277)	108.7(397)	**82.8(215)**	130.6(385)	138.6(286)
%[c]	62.8	45.6	83.6	43.6	**0.8**	68.8	77.2

U7C and d-U7C are considered as control simulations as it has been shown that U7C mutation has almost no effect on the catalysis [74]. Distance and angles (Figure 5) are in angstrom and degrees, respectively. Standard deviations (SDs) are listed in parenthesis divided by the decimal precision of the average (e.g., if the number is reported to two digits of decimal precision, the SD is divided by 0.01). Boldface font is used to highlight key quantities that are significantly altered with respect to the wild-type (WT) simulation upon mutation and that are discussed in the text.

[a] In-line fitness index [75].

[b] The $N_3 \ldots N_1$ distance between nucleobases in the 3 and 8 positions.

[c] The hydrogen-bond contact percentage of the general acid with the leaving group defined as the percentage of the snapshots in which $r_{HA} \leq 3.0$ Å and $\theta_{HA} \geq 120°$.

[d] The notation "d-" denotes the activated precursor-state simulations having the C17:$O_{2'}$ deprotonated.

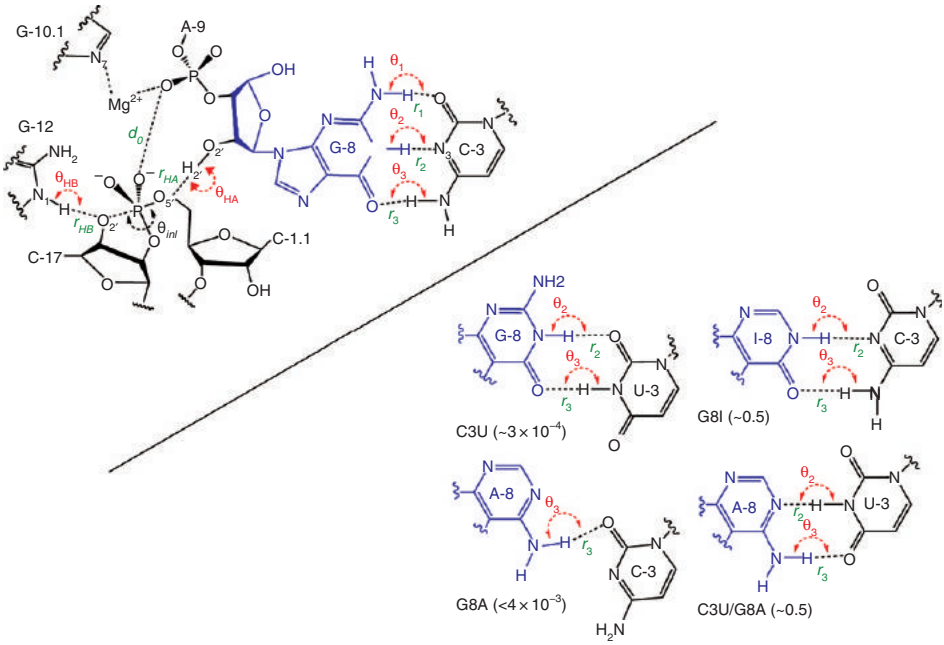

Figure 5 Upper: Active site of the full-length hammerhead RNA using the canonical minimal sequence numbering scheme described in [40] and [42]. Lower: Representative hydrogen bonding of the C3:G8 base pair observed from mutant simulations. Experimental relative catalytic rates of mutant versus wild-type minimal sequence ribozymes $(k_{\mathrm{mut}}/k_{\mathrm{wt}})$ are shown in parentheses (C3U from [76], G8A from [78], C3U/G8A from [73], and G8I from [34]), and may differ for the full-length sequence.

acid). These perturbations in the reactant state would prevent activation of the nucleophile and progress toward the TS. Experimental evidence shows that C3U indeed reduces the rate constant by more than three orders of magnitude [76].

G8A mutation disrupts the positioning of G8:$O_{2'}$ as general acid in the activated precursor. The G8A mutation reduces the catalytic rate by a factor 0.004 [78]. Simulation results indicate that the G8A mutation considerably weakens the base pair with C3 with only one weak hydrogen bond that remains intact (Figure 5). In the reactant-state simulation, G8A does not appear to dramatically alter the active site contacts relative to the wild-type simulation, with the exception of the A8:N_1…C3:N_3 distance which increases due to a shift in the hydrogen-bond pattern (Figure 5). In the activated precursor state, however, the hydrogen bond positioning between G8:$H_{2'}$ and C1.1:$O_{5'}$ is significantly disrupted relative to the wild- type simulation. The G8A mutation shifts the conserved 2′OH of G8 away from the ideal general acid position and can possibly block the general acid step of the reaction. Mutation of G8 to 2-aminopurine (AP) [34,78] or to 2,6-diaminopurine (diAP) [78], which are expected to have similarly weakened hydrogen bonding as the G8A mutation reduces the reaction rate by over three orders of magnitude.

G8I and C3U/G8A mutations are relatively benign. Whereas the relatively isosteric C3U and G8A mutations lead to considerably reduced catalytic rates, the G8I [34,78] and C3U/G8A [73] mutations affect the rate by less than an order of magnitude. The C3U/G8A double mutation and G8I single mutation simulations indicate that the hydrogen-bond network retains the overall base positions relative to the wild-type simulation and suggest that these two mutations do not significantly alter any of the active site indexes that would affect activity relative to the wild-type simulation (Table 4).

Structural deviations that give rise to mutation effects can occur at different stages along the reaction path. Although the canonical Watson–Crick hydrogen-bond network is altered significantly in both C3U and G8A mutations, the simulations suggest that the origin of the mutational effect on the ribozyme kinetics can occur at different stages along the reaction path. In the reactant state, the Mg^{2+} ion is bound between G10.1:N_7 and A9:O_{2P}. The large base-pair shift that occurs in the C3U mutation simulation results in compromise of the active site structure, including the loss of interactions between the proposed general base and the nucleophile. In the activated precursor state, the Mg^{2+} ion occupies a bridging position between A9:O_{2P} and the scissile phosphate. The G8A mutation, which is very weakly hydrogen bonded, does not sustain a catalytically viable position of the general acid.

Hydrogen bonding between nucleobases in the 3 and 8 positions is necessary but not sufficient to preserve active site structural integrity. The G8I and C3U/G8A mutations that largely preserve a stable base-pair hydrogen-bonded scaffold lead to relatively benign mutations. A C3G/G8C base-pair switch mutation that preserves hydrogen-bonded base pairing partially rescues activity relative to the single mutations, although still reduces activity by 150–200-fold [41,79]. Recent analysis of all base-pair mutations indicate considerable variation in activity, but all of the nonnative mutations at this position are considerably less active [79]. The present simulation results offer the prediction that whereas both C3U [76] and G8diAP [78] single mutations are observed experimentally to reduce catalytic activity by several orders of magnitude, a correlated C3U/G8diAP double mutation, which retains base-pair hydrogen bonding, should exhibit a partial rescue effect in the HHR.

3. MOLECULAR SIMULATIONS OF THE L1 LIGASE

In this section, we show how large-scale MD simulations together with crystallographic data were able to reveal the dynamical hinge points of L1L. We have performed a series of MD simulations of L1L in explicit solvent to examine to what degree the two crystallized conformers persist as stable conformational intermediates in solution and examine the nature of the inactive–active conformational switch. Four simulations were performed departing from each conformer in both the reactant and product states, in addition to a simulation where local unfolding in the active state was induced. From these simulations, a set of four virtual torsion angles that span two evolutionarily conserved and restricted

regions were identified as dynamical hinge points in the conformational switch transition. The ligation site visits three distinct states characterized by hydrogen-bond patterns that are correlated with the formation of specific contacts that may promote catalysis. The insights gained from these simulations contribute to a more detailed understanding of the coupled catalytic/conformational switch mechanism of L1L that may facilitate the design and engineering of new catalytic riboswitches. The following simulations have been run:

- **Prod-D**: product in the docked conformation
- **Prod-D-UF**: product in the docked conformation–forced unfolding
- **Prod-U**: product in the undocked conformation
- **Prec-D-XTP**: reactant precursor in the docked conformation and the triphosphate in extended conformation
- **Prec-D-MgTP**: reactant precursor in the docked conformation and the triphosphate in an extended conformation coordinated with a Mg^{2+} ion

3.1 Conformational variation of L1L occurs at dynamical hinge points

Figure 6 illustrates the crystallographic presumably active "docked" and inactive "undocked" conformers. Most of the structural variation is observed in the junction region connecting the stems where the RMSD between crystal conformers is 8.30 Å. This variation in the junction propagates to a large-scale swing of stem C by around 80 Å in arc length. Individually, L1L stems (A, B, and C), as found in the crystal structure, show small deviations (RMSD 1.71, 0.71, and 2.06 Å, respectively) between the docked and undocked conformational states, and the internal base-pair hydrogen-bonding patterns are completely conserved between conformers.

The two crystallographic conformers can be distinguished by changes in their virtual torsion angles (Figure 7) [66,67]. A survey of the 142 virtual torsion angles in L1L reveals that only four show a significant change (>45°): θ_{18}, θ_{37}, θ_{44}, and η_{38} (Figure 7). These torsions span regions that contain the evolutionarily conserved residues: U37, U38, A39 for θ_{37} and η_{38} and the 5-base motif (C39=G18 G37 A38 C17/U39=A38 U37 G38 U17) and the neighboring U19 for θ_{18} and θ_{44} [62].

Both U38 and U19 are of particular interest in the current work: U38 contributes to the docking of stem C into stem A in the active conformation and mutation data demonstrates that it is critical for catalysis, and U19 is evolutionarily conserved (97%), although its role in catalysis remains unclear [55,61–63]. In both crystallographic conformers, U19 is oriented toward the exterior of the L1L body without making any contacts. The lack of clear structural basis that explains the conserved character of U19 in either the docked or undocked crystal structures motivates the question as to whether this residue might be important in facilitating the undocked to docked conformational switch.

Large fluctuations in the three-way junction suggest the presence of dynamical hinge points. In the Prod-D and Prod-U simulations, the virtual torsions associated with the residues that form the junction region (J) are characterized by a residue-average standard deviation (RASD) of 16.1° and 18.5°, respectively,

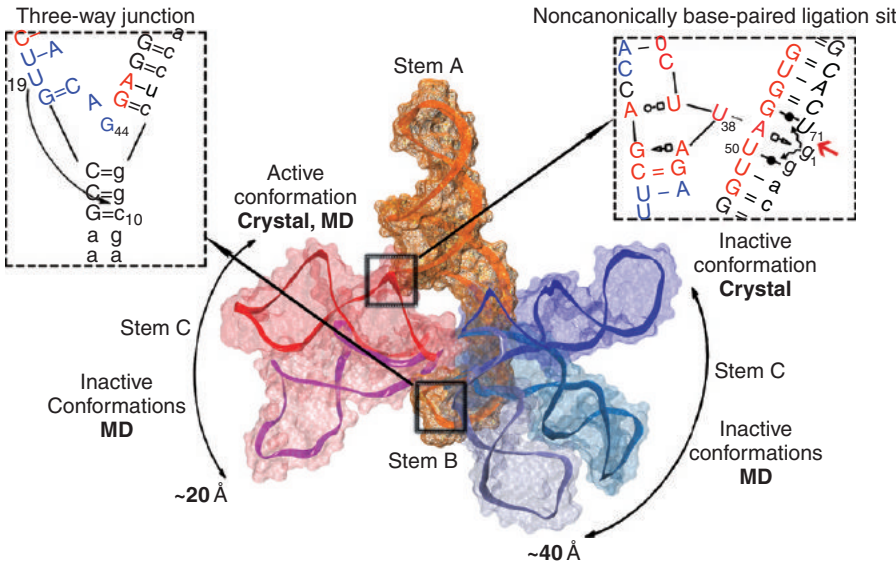

Figure 6 Representative snapshots from the simulations illustrating the coupled on–off conformational switch-catalytic pathway starting from the active and inactive conformations, in both precursor and product states. Middle: Representative snapshots from the simulations are shown with stems A and B (in yellow wireframe surface) aligned and C in ribbons with transparent surfaces. Left panel: Contacts important for stabilization of intermediate states that involve the conserved U_{19} and stem B. Right panel: Interaction patterns for three states observed in the simulations between G_1/GTP_1 and the noncanonically base-paired ligation site. The states that do not appear in the crystal structure are indicated with curly arrows. (For interpretation of the references to colour in this figure legend, the reader is referred to the web version of this book.)

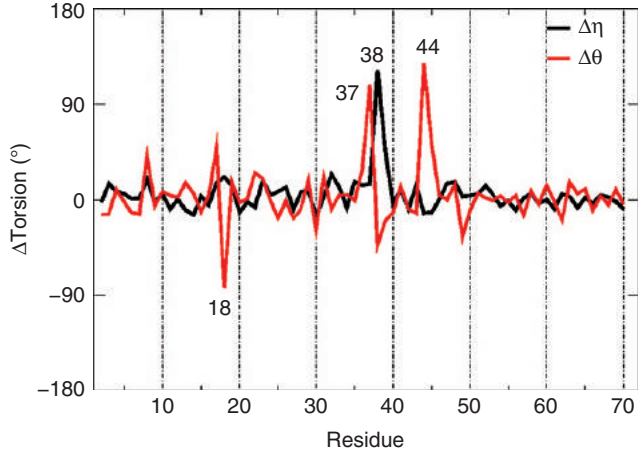

Figure 7 Variations of the virtual torsions (Δ*Torsion*, where *Torsion* indicates either η or θ) between the docked (active) and undocked (inactive) conformers as found in the crystal structure. The $\Delta\eta$ (black) and $\Delta\theta$(red) are shown. Only four virtual torsions, θ_{19}, θ_{37}, η_{38}, and η_{44} show significant deviations (80.0° or more), whereas all other virtual torsions show relatively minor changes (typically less than 25.0°). (For interpretation of the references to colour in this figure legend, the reader is referred to the web version of this book.)

whereas the RASD for the canonically base-paired stem A, for example, is ~12.5° for the Prod-U simulation. Similar values are found for the other stems. This suggests that the junction possesses a higher degree of intrinsic flexibility relative to other regions of the L1L.

The major contributors (SD $\geq$ 30.0) to these large values of RASD are θ_{44} (SD 48.7°) and η_{45} (SD 71.0°) for the Prod-D simulation, and θ_{18} (SD 56.8°), η_{19} (SD 30.7°), θ_{19} (SD 37.8°), η_{20} (SD 53.6°), and θ_{20} (SD 30.8°) for the Prod-U simulation. In the case of the Prod-D-UF simulation, θ_{44} and η_{45} virtual torsions have the largest standard deviations in the junction region (~30.0°).

A possible connection can be made between these relatively large fluctuations of some of the virtual torsions that span the junction region and the transition from the inactive to the active conformation. For example, during Prod-U simulation (370 ns), θ_{18} is observed to transition through a series of two relatively distant clusters that are disposed exactly on the same path that would allow the undocked$\rightleftharpoons$docked conformational transformation to occur as apparent from the crystal structure.

During the same simulation, the conserved U19 can be observed interacting specifically with stem B, accounting for its possible role in the stabilization of intermediate states on the conformational transition pathway. These interaction patterns that correlate with the transition along the θ_{18} virtual torsion were observed and involve a variety of base–base, base–backbone, or backbone–backbone hydrogen bonds. Given the conserved nature of the interacting partners, it is possible that these base–base interactions play an important role in the stabilization of the intermediate states during transitions between the two conformations, and contribute in part to the discrimination in the evolutionary optimization process between active and inactive constructs.

3.2 The U38 loop responsible for allosteric control is intrinsically flexible

The fact that U_{38}, a conserved residue critical for catalytic activity in the L1L family, is docked into the ligation site and makes a canonical base pair with a constituent of the ligation site A51 in the docked conformation, whereas in the undocked conformation it is positioned ~40 Å away from the site, has led to the postulate that the former is more likely representative of a catalytically active state [64].

In the crystal structures, the conformation of the U38 loop varies considerably between the docked and undocked conformers, showing two different conformations. Two virtual torsions that span the loop, θ_{37} and η_{38}, show a large variation (~120.0°) between the two crystal conformers, whereas all the other virtual torsions in the immediate base-paired vicinity show much smaller variation (20.0°) (Figure 7). Mechanistically, during the undocked$\rightleftharpoons$docked conformational transition, the U38 loop has to transition from a state where U38 is buried into stem C and makes a sugar-base hydrogen bond with A23 into an open conformation that will expose U38 in solution giving it the possibility to dock

into stem A. The docking consists in the formation of a canonical base U38=A52 and several phosphate–Mg^{2+} contacts, supported by A39 and G40 of stem C on one side and G1 of stem A on the other.

In the Prod-D, Prec-D-XTP and Prec-D-MgTP simulations, U38 remains base paired with A51, and the overall behavior of the θ_{37} and η_{38} virtual torsions is similar. For the Prod-D simulation, the average values for the θ_{37} and η_{38} torsions (220.3° and 27.0°, respectively) stay within 43° of the values found in the docked crystal conformer (243.8° and –15.5°, respectively). In the Prod-U simulation, the θ_{37} and η_{38} virtual torsions follow a similar trend with respect to their undocked conformer values. Averages were 192.1° and 128.7°, respectively, compared to 135.9° and 105.9° in the undocked crystal structure. For these set of simulations (Prod-D, Prec-D-XTP, Prec-D-MgTP and Prod-U), U_{38} fluctuates relatively close to its starting geometry in two approximately separate states indicated with different colors in Figure 8b (lower panel). These two regions are labeled D (solvent exposed/docked) and U (buried), respectively, and two representative structures are depicted in Figure 8a. As shown by the correlation plots of θ_{37} and η_{38} virtual torsions (Figure 8b, upper panel) in the Prod-D-UF simulation, the U_{38} loop is able to span the conformational space that covers almost exactly the same area that includes the reunion of the regions sampled during Prod-D and Prod-U simulations, encompassing the conformations found in crystal.

3.3 Anatomy of the ligation site and implications for catalysis

L1L catalyzes the phosphodiester-bond formation between GTP1:P_α and U71:$O_{3'}$. Generally, this type of nucleotidyl transfer reaction proceeds through a pentacovalent TS or metastable intermediate that causes the inversion of the P_α stereochemistry and results in the release of pyrophosphate [80,81]. The noncanonically base-paired ligation site on stem A is built from three non-canonical base pairs: U50•G2 (cis-WC/WC), A51□→G1 (trans-Hoogsteen/sugar edge), and G52•U71(cis-WC/WC) (Figure 6, right inset). In the crystallographic docked product conformation, A51 is also involved in a canonical base pair with U38 giving rise to base triple U38–A51□→G1. This interaction along with the interactions between G1, A39, and G40 phosphates with a Mg^{2+} ion is responsible for mediating the docking of stem C into stem A. The formation of the base triple U38–A51□→G1 disrupts the hydrogen bond between G1:O2′ and A51:N6. This hydrogen bond is present in the undocked conformer crystal structure and is typical for a trans-Hoogsteen/sugar edge base pair [82].

During the Prod-D, Prec-XTP, and Prec-MgTP simulations, the ligation site shows a strong variability, spanning a series of three conformational clusters characterized by the formation of specific hydrogen bond interactions between G1/GTP1 and the rest of the ligation site. G1/GTP1 oscillates between (Figure 9) formation of hydrogen bond with G52, GTP1/G1:N2–G52:O6 (cluster 1), a base triple with A51 and U38 that is identical to that found in crystallized docked conformer (cluster 2), and a base triple with U50 and G2 (cluster 3).

One of the structural features that confers an increased flexibility for G1/GTP1 and its ability to interact with different parts of the ligation site for

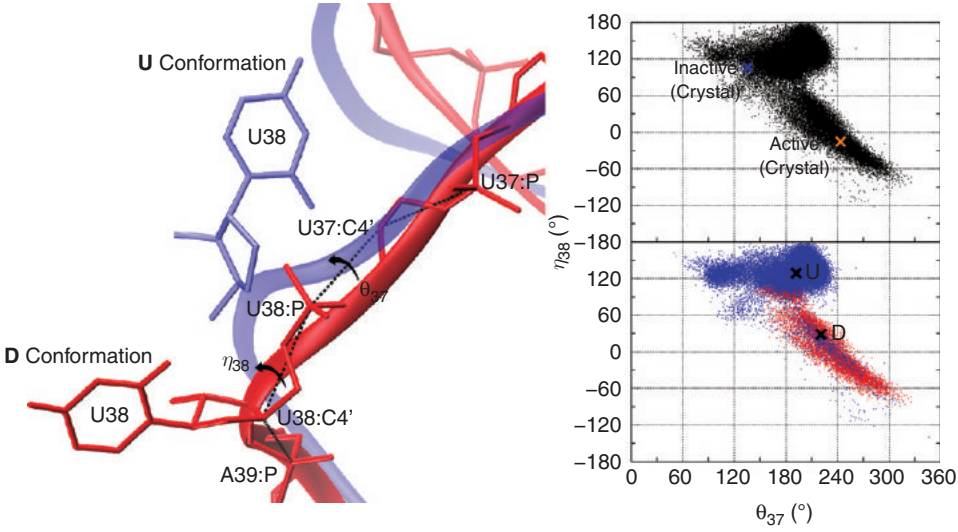

Figure 8 The U_{38} loop is responsible for allosteric control of the catalytic step by transitioning from a "closed" conformation, labeled "U conformation" (specific, as shown by our simulations, to the inactive/undocked conformers), to an "open" conformation, labeled "D conformation" (specific to the active/docked conformations). (Left) Representative conformations for the U and D conformations. (Right) Upper panel: During Prod-D-UF simulation, where unfolding of the docked state was induced by removal of key interstem interactions, the complete transition between the two states was observed by monitoring θ_{37} and η_{38} virtual torsions. The values of the θ_{37} and η_{38} found in the two crystallized conformers are shown with blue and orange crosses. Lower panel: The θ_{37}/η_{38} space sampled in the Prod-D-UF overlaps with regions sampled during the Prod-D (red) and Prod-U (blue) simulations. The center of each distribution is marked with black crosses. (For interpretation of the references to colour in this figure legend, the reader is referred to the web version of this book.)

the Prod-D, Prec-XTP, and Prec-MgTP simulations resides in the way GTP1/G1:$O_{2'}$ interacts with the ligation site and the solvent. During Prod-D, Prec-XTP, and Prec-MgTP simulations, GTP1/G1:$O_{2'}$ shows no tendency to recover the G1:$O_{2'}$–A51:N_6 hydrogen bond present in the undocked crystal and Prod-U simulation, but instead interacts alternately with bulk water molecules or G2:O_{2P}. Docking of stem C into stem A causes the rupture of the G1:$O_{2'}$–A51:N6 hydrogen bond in the active state and has the effect of increasing the degree of conformational variability in the ligation site of the product and precursor/reactant state.

During the simulations, the nucleophile U71:$H_{O3'}$ is involved in contacts with U71:$O_{2'}$ and GTP1:$O_{2P\alpha}$, where the latter is positioned to possibly act as a general base. These hydrogen bonds are mainly formed from structures in clusters 1 and 3, with negligible probability for cluster 2, as shown in Figure 9. The variability of the ligation site (i.e., the capacity to visit several conformational clusters) makes it possible to induce the formation of specific contacts that might promote the chemical step in catalysis (i.e., the contact between U71:$H_{O3'}$ and GTP1:O_{2P}). This is due to the noncanonical base pairing of the ligation site.

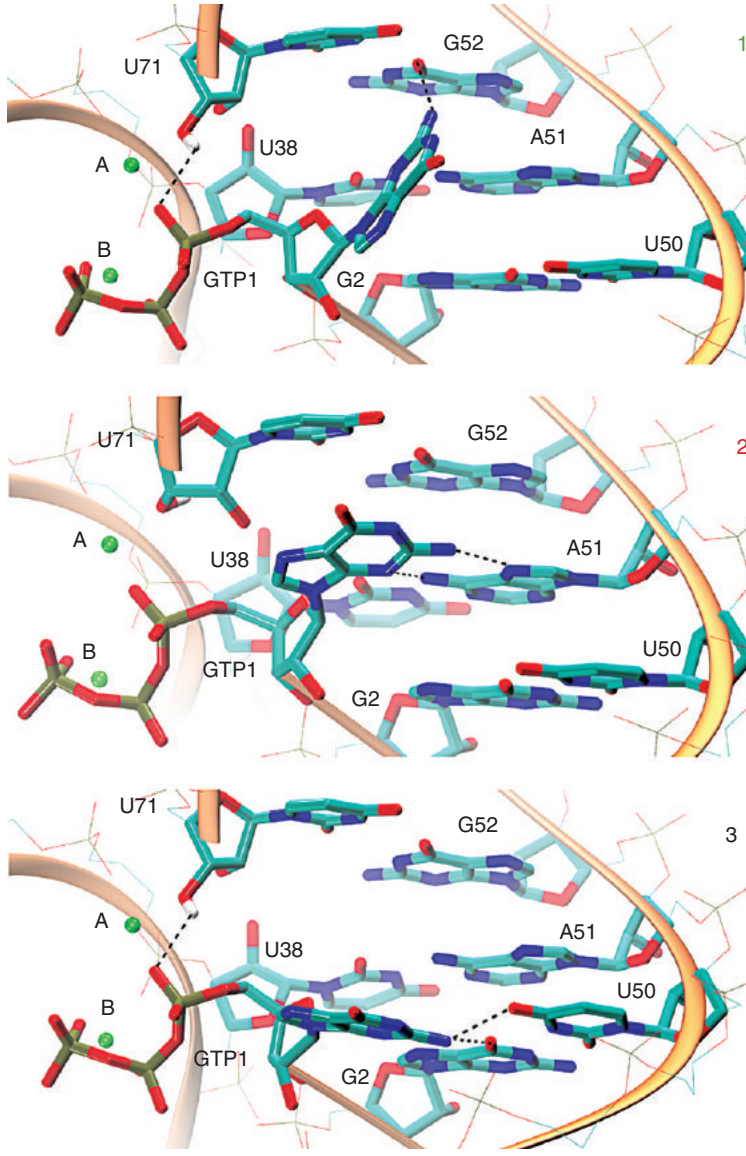

Figure 9 The noncanonically base-paired ligation site exhibits a high degree of conformational variability, passing through a series of three states (clusters 1, 2, and 3) characterized by specific hydrogen-bond patterns between GTP1/G1 and the ligation site. The arrangement of the ligation site in the case of the Prec-MgTP simulations is shown.

4. METHODS

Simulations were performed with the NAMD simulation package (version 2.6) [83] using the all-atom Cornell et al. force field (parm99) [84], generated with the AMBER 10 package [85–87] and TIP3P water model [88]. Periodic boundary

conditions were used along with the isothermal–isobaric ensemble (*NPT*) at 1 atm and 300 K using Nosé–Hoover–Langevin pressure piston control [89,90] with a decay period of 100.0 fs and a damping time scale of 50 fs, and the Langevin thermostat with a damping coefficient of 0.1 ps^{-1}. The smooth particle mesh Ewald (PME) method [91,932] was employed with a B-spline interpolation order of 6 and the default value used in NAMD. The fast Fourier transform (FFT) grid points used for the lattice directions were chosen using ~1.0 Å spacing. Nonbonded interactions were treated using an atom-based cutoff of 12.0 Å with switching of nonbond potential beginning at 10.0 Å. Numerical integration was performed using the leap-frog Verlet algorithm with 1 fs time step [93]. Covalent bond lengths involving water hydrogens were constrained using the SHAKE algorithm [94].

For the QM/MM simulations, the system is partitioned into a QM region constituting the active site that is represented by the AM1/d-PhoT Hamiltonian [95] and the modified AM1 magnesium parameters of Hutter and coworkers [96]. The simulations were performed with CHARMM [97] (version c32a2) using the all-atom CHARMM27 nucleic acid force field [98,99] with extension to reactive intermediate models (e.g., TS mimics) [72]. The generalized hybrid orbital (GHO) method [100] is used to cut a covalent bond to divide the system into QM and MM region. Full electrostatic interactions were calculated using a recently introduced linear-scaling QM/MM-Ewald method [101].

5. CONCLUSION

In this chapter, we summarized our progress toward the understanding of HHR and L1L ribozyme catalysis through a multiscale simulation strategy. This strategy employs long-time MD simulations using a classical MM force field in explicit solvent and specialized MM residues for metal ion interactions and reactive intermediates. Additionally, we employed a set of shorter time simulations using a combined QM/MM potential that uses a recently developed semiempirical QM model for phosphoryl transfer reactions that was derived from high-level density-functional calculations of reactions important in RNA catalysis. Long-range ionic interactions were treated rigorously with linear-scaling electrostatic methods for periodic systems.

Simulation results for the HHR paint a picture of its catalysis that includes a novel role for a catalytic metal ion. The HHR folds to form an electrostatic negative pocket to recruit a threshold occupation of cationic charge, either a Mg^{2+} ion or multiple monovalent ions when Mg^{2+} ions are not present. The position and coordination pattern of these ions are important for formation of active in-line attack conformations. In the case of single Mg^{2+} ion bound in the active site, the Mg^{2+} ion initially stays at the C-site in the reactant state and migrates to a bridging position (the B-site) after the nucleophile (C17:$O_{2'}$) is deprotonated. As the reaction proceeds, the Mg^{2+} ion can stabilize the accumulating charge of the leaving group and bind to the general acid (G8:$O_{2'}$), significantly increasing its ability to act as a general acid catalyst to transfer a proton to

the leaving group (C1.1:$O_{5'}$). Our QM/MM studies demonstrate that the Mg^{2+} ion not only facilitates the protonation of the leaving $O_{5'}$, but also plays an important role in the final dissociation step of the catalysis. The mutational simulation results are consistent with observed mutational data and suggest that the active site fold is well tuned for the reaction and most disruptions due to mutations have severe impact on the HHR catalysis that can occur at different stages of the reaction.

Simulation results for the L1L ribozyme have identified important dynamical hinge points in the conformational transition from inactive to active forms of the L1L and characterized interactions that stabilize intermediates along the transition pathway. From the simulations, we have identified a reduced set of four virtual torsions that span two evolutionarily conserved and restricted regions located in the three-way junction and can be used to distinguish between the active and inactive conformations found in crystal. Analysis of the structure and dynamics of the noncanonically base-paired active site have implications for catalysis. Simulations were performed from two different initial arrangements of the reactant state differing in the conformation of the GTP_1 triphosphate and its Mg^{2+} coordination. The U71:$O_{3'}$ nucleophile was observed to make direct hydrogen bond interactions with the O_2 of GTP_1, in support of the role of this residue as a potential general base. These studies advance our knowledge of the coupled catalytic/conformational riboswitch mechanism of L1L and may have broader implications for understanding the function of prebiotic RNA enzymes.

The present work uses molecular simulations to provide a deeper understanding into how structure and dynamics affect catalysis in the HHR and L1L ribozyme. In particular, the role of conformational transitions and metal ion binding is explored. The insights gained from these studies provide guiding principles into catalysis of a archetype ribozyme and a novel catalytic riboswitch that may have broader implications for prebiotic RNA enzymes, and ultimately facilitate the design of new RNA-based biomedical technology. Still much work, both experimental and theoretical, is needed to obtain a consensus view of the detailed mechanism, for which the present study provides important groundwork and progress.

ACKNOWLEDGMENTS

We are grateful for financial support provided by the National Institutes of Health (GM62248 for the HHR studies and GM084149 for the L1L studies). This work was supported in part by the University of Minnesota Biomedical Informatics and Computational Biology program (TL and DY) and by a generous allocation on an IBM Blue Gene BG/P with 4,096 850 Mhz CPUs at the IBM Advanced Client Technology Center in Rochester, Minnesota, with further thanks to Cindy Mestad, Steven Westerbeck, and Geoffrey Costigan for technical assistance. This research was also performed in part using the Molecular Science Computing Facility (MSCF) in the William R. Wiley Environmental Molecular Sciences Laboratory, a national scientific user facility sponsored by the U.S. Department of Energy's Office of Biological and Environmental Research and located at the Pacific Northwest National Laboratory, operated for the Department of Energy by Battelle. Computational resources from The Minnesota Supercomputing Institute for Advanced Computational Research (MSI) were utilized in this work.

REFERENCES

1. Chen, X., Li, N., Ellington, A.D. Ribozyme catalysis of metabolism in the RNA world. Chem. Biodivers. 2007, 4, 633–55.
2. Gesteland, R.F., Cech, T.R., Atkins, J.F. The RNA World: The Nature of Modern RNA Suggests a Prebiotic RNA, 2nd edn., Cold Spring Harbor Laboratory Press, New York, 1999.
3. Gilbert, W. The RNA world. Nature 1918, 319, 618.
4. Lilley, D.M. In Ribozymes and RNA Catalysis. RSC Biomolecular Series (eds D.M. Lilley and F. Eckstein), RSC Publishing, Cambridge, 2008, pp. 66–91.
5. Scott, W.G. Molecular palaeontology: Understanding catalytic mechanisms in the RNA world by excavating clues from a ribozyme three-dimensional structure. Biochem. Soc. Trans. 1996, 24(3), 604–8.
6. Scott, W.G. Ribozymes. Curr. Opin. Struct. Biol. 2007, 17, 280–6.
7. Yarus, M. Boundaries for an RNA world. Curr. Opin. Chem. Biol. 1999, 3, 260–7.
8. Breaker, R.R. Engineered allosteric ribozymes as biosensor components. Curr. Opin. Biotechnol. 2002, 13(1), 31–9.
9. Rubenstein, M., Tsui, R., Guinan, P. A review of antisense oligonucleotides in the treatment of human disease. Drugs Future 2004, 29, 893–909.
10. Vaish, N.K., Dong, F., Andrews, L., Schweppe, R.E., Ahn, N.G., Blatt, L., Seiwert, S.D. Monitoring post-translational modification of proteins with allosteric ribozymes. Nat. Biotech. 2002, 20, 810–5.
11. McDowell, S.E., Špačková, N., Šponer, J., Walter, N.G. Molecular dynamics simulations of RNA: An in silico single molecule approach. Biopolymers 2007, 85, 169–84.
12. Gao, J. Methods and applications of combined quantum mechanical and molecular mechanical potentials. Rev. Comput. Chem. 1995, 7, 119–85.
13. Monard, G., Merz, K.M., Jr. Combined quantum mechanical/molecular mechanical methodologies applied to biomolecular systems. Acc. Chem. Res. 1999, 32, 904–11.
14. Senn, H.M., Thiel, W. QM/MM studies of enzymes. Curr. Opin. Chem. Biol. 2007, 11, 182–7.
15. Warshel, A. Molecular dynamics simulations of biological reactions. Acc. Chem. Res. 2002, 35, 385–95.
16. Warshel, A. Computer simulations of enzyme catalysis: Methods, progress, and insights. Annu. Rev. Biophys. Biomol. Struct. 2003, 32, 425–43.
17. Norberg, J., Nilsson, L. Molecular dynamics applied to nucleic acids. Acc. Chem. Res. 2002, 35, 465–72.
18. Orozco, M., Noy, A., Pérez, A. Recent advances in the study of nucleic acid flexibility by molecular dynamics. Curr. Opin. Struct. Biol. 2008, 18(2), 185–93, http://dx.doi.org/10.1016/j.sbi.2008.01.005
19. Orozco, M., Pérez, A., Noy, A., Luque, F.J. Theoretical methods for the simulation of nucleic acids. Chem. Soc. Rev. 2003, 32, 350–64.
20. Auffinger, P., Hashem, Y. Nucleic acid solvation: From outside to insight. Curr. Opin. Struct. Biol. 2007, 17(3), 325–33, http://dx.doi.org/10.1016/j.sbi.2007.05.008.
21. Cheatham, T.E., III Simulation and modeling of nucleic acid structure, dynamics and interactions. Curr. Opin. Struct. Biol. 2004, 14, 360–7.
22. Chen, S.-J. RNA folding: Conformational statistics, folding kinetics, and ion electrostatics. Annu. Rev. Biophys. 2008, 37, 197–214, http://dx.doi.org/10.1146/annurev.biophys.37.032807.125957.
23. Blount, K.F., Uhlenbeck, O.C. The hammerhead ribozyme. Biochem. Soc. Trans. 2002, 30(Pt 6), 1119–22, http://dx.doi.org/10.1042/.
24. Scott, W.G. Biophysical and biochemical investigations of RNA catalysis in the hammerhead ribozyme. Q. Rev. Biophys. 1999, 32, 241–94.
25. Doherty, E.A., Doudna, J.A. Ribozyme structures and mechanisms. Annu. Rev. Biophys. Biomol. Struct. 2001, 30, 457–75.
26. Scott, W.G. RNA catalysis. Curr. Opin. Struct. Biol. 1998, 8(6), 720–6.
27. Michienzi, A., Cagnon, L., Bahner, I., Rossi, J.J. Ribozyme-mediated inhibition of HIV 1 suggests nucleolar trafficking of HIV-1 RNA. Proc. Natl. Acad. Sci. U.S.A. 2000, 97(16), 8955–60.

28. Sarver, N., Cantin, E.M., Chang, P.S., Zaia, J.A., Ladne, P.A., Stephens, D.A., Rossi, J.J. Ribozymes as potential anti-HIV-1 therapeutic agents. Science 1990, 247, 1222–5.
29. Snyder, D.S., Wu, Y., Wang, J.L., Rossi, J.J., Swiderski, P., Kaplan, B.E., Forman, S.J. Ribozyme-mediated inhibition of bcr-abl gene expression in a Philadelphia chromosome-positive cell line. Blood 1993, 82(2), 600–5.
30. Feng, Y., Kong, Y.Y., Wang, Y., Qi, G.R. Intracellular inhibition of the replication of hepatitis B virus by hammerhead ribozymes. J. Gastroenterol. Hepatol. 2001, 16(10), 1125–30.
31. Weinberg, M., Passman, M., Kew, M., Arbuthnot, P. Hammerhead ribozyme-mediated inhibition of hepatitis b virus x gene expression in cultured cells. J. Hepatol. 2000, 33(1), 142–51.
32. Sano, M., Taira, K. Hammerhead ribozyme-based target discovery. Methods Mol. Biol. 2007, 360, 143–53, http://dx.doi.org/10.1385/1-59745-165-7:143
33. Martick, M., Horan, L.H., Noller, H.F., Scott, W.G. A discontinuous hammerhead ribozyme embedded in a mammalian messenger RNA. Nature 2008a, 454(7206), 899–902, http://dx.doi.org/10.1038/nature07117.
34. Blount, K.F., Uhlenbeck, O.C. The structure-function dilemma of the hammerhead ribozyme. Annu. Rev. Biophys. Biomol. Struct. 2005, 34, 415–40.
35. Takagi, Y., Ikeda, Y., Taira, K. Ribozyme mechanisms. Top. Curr. Chem. 2004, 232, 213–51.
36. Suzumura, K., Takagi, Y., Orita, M., Taira, K. NMR-based reappraisal of the coordination of a metal ion at the Pro-Rp oxygen of the A9/G10.1 site in a hammerhead ribozyme. J. Am. Chem. Soc. 2004, 126(47), 15504–11.
37. Wang, S., Karbstein, K., Peracchi, A., Beigelman, L., Herschlag, D. Identification of the hammerhead ribozyme metal ion binding site responsible for rescue of the deleterious effect of a cleavage site phosphorothioate. Biochemistry 1999, 38(43), 14363–78.
38. Murray, J.B., Szöke, H., Szöke, A., Scott, W.G. Capture and visualization of a catalytic RNA enzyme-product complex using crystal lattice trapping and X-ray holographic reconstruction. Mol. Cell 2000, 5, 279–87.
39. Murray, J.B., Terwey, D.P., Maloney, L., Karpeisky, A., Usman, N., Beigelman, L., Scott, W.G. The structural basis of hammerhead ribozyme self-cleavage. Cell 1998, 92, 665–73.
40. Scott, W.G., Murray, J.B., Arnold, J.R.P., Stoddard, B.L., Klug, A. Capturing the structure of a catalytic RNA intermediate: The hammerhead ribozyme. Science 1996, 274, 2065–9.
41. Martick, M., Scott, W.G. Tertiary contacts distant from the active site prime a ribozyme for catalysis. Cell 2006, 126(2), 309–20.
42. Martick, M., Lee, T.-S., York, D.M., Scott, W.G. Solvent structure and hammerhead ribozyme catalysis. Chem. Biol. 2008, 15, 332–42.
43. Lee, T.-S., Giambau, G.M., Sosa, C.P., Martick, M., Scott, W.G., York, D.M. Threshold occupancy and specific cation binding modes in the hammerhead ribozyme active site are required for active conformation. J. Mol. Biol. 2009, 388, 195–206. http://dx.doi.org/10.1016/j.jmb.2009.02.054.
44. Lee, T.-S., Silva Lopez, C., Giambasu, G.M., Martick, M., Scott, W.G., York, D.M. Role of Mg^{2+} in Hammerhead ribozyme catalysis from molecular simulation. J. Am. Chem. Soc. 2008, 130(10), 3053–64.
45. Lee, T.-S., Silva-Lopez, C., Martick, M., Scott, W.G., York, D.M. Insight into the role of Mg^{2+} in hammerhead ribozyme catalysis from x-ray crystallography and molecular dynamics simulation. J. Chem. Theory Comput. 2007, 3, 325–7.
46. Lee, T.-S., York, D.M. Origin of mutational effects at the C3 and G8 positions on hammerhead ribozyme catalysis from molecular dynamics simulations. J. Am. Chem. Soc. 2008, 130(23), 7168–9.
47. Scott, W.G. Morphing the minimal and full-length hammerhead ribozymes: Implications for the cleavage mechanism. Biol. Chem. 2007, 388, 727–35.
48. Joyce, G.F. A glimpse of biology's first enzyme. Science 2007, 315, 1507–8.
49. Bartel, D.P., Szostak, J.W. Isolation of new ribozymes from a large pool of random sequences. Science 1993, 261(5127), 1411–8.
50. Bagby, S.C., Bergman, N.H., Shechner, D.M., Yen, C., Bartel, D.P. A class I ligase ribozyme with reduced Mg^{2+} dependence: Selection, sequence analysis, and identification of functional tertiary interactions. RNA 2009, 15, 2129–46.

51. Ekland, E.H., Szostak, J.W., Bartel, D.P. Structurally complex and highly active RNA ligases derived from random RNA sequences. Science 1995, 269, 364–9.
52. Ikawa, Y., Tsuda, K., Matsumura, S., Inoue, T. De novo synthesis and development of an RNA enzyme. Proc. Natl. Acad. Sci. U.S.A. 2004, 101, 13750–5.
53. Jaeger, L., Wright, M.C., Joyce, G.F. A complex ligase ribozyme evolved *in vitro* from a group I ribozyme domain. Proc. Natl. Acad. Sci. U.S.A. 1999, 96, 14712–7.
54. McGinness, K.E., Joyce, G.F. In search of an RNA replicase ribozyme. Chem. Biol. 2003, 10(1), 5–14.
55. Robertson, M.P., Ellington, A.D. *In vitro* selection of an allosteric ribozyme that transduces analytes to amplicons. Nat. Biotech. 1999, 17, 62–6.
56. Rogers, J., Joyce, G.F. A ribozyme that lacks cytidine. Nature 1999, 402, 323–5.
57. Shechner, D.M., Grant, R.A., Bagby, S.C., Koldobskaya, Y., Piccirilli, J.A., Bartel, D.P. Crystal structure of the catalytic core of an RNA-polymerase ribozyme. Science 2009, 326, 1271–5.
58. Landweber, L.F., Pokrovskaya, I.D. Emergence of a dual-catalytic RNA with metal-specific cleavage and ligase activities: The spandrels of RNA evolution. Proc. Natl. Acad. Sci. U.S.A. 1999, 96, 173–8.
59. Ellington, A.D., Szostak, J.W. *In vitro* selection of RNA molecules that bind specific ligands. Nature 1990, 346(6287), 818–22. http://dx.doi.org/10.1038/346818a0.
60. Marshall, K.A., Ellington, A.D. Training ribozymes to switch. Nat. Struct. Biol. 1999, 6(11), 992–4.
61. Robertson, M.P., Ellington, A.D. Design and optimization of effector-activated ribozyme ligases. Nucleic Acids Res. 2000, 28, 1751–9.
62. Robertson, M.P., Ellington, A.D. *In vitro* selection of nucleoprotein enzymes. Nat. Biotech. 2001, 19, 650–5.
63. Robertson, M.P., Knudsen, S.M., Ellington, A.D. *In vitro* selection of ribozymes dependent on peptides for activity. RNA 2004, 10, 114–27.
64. Robertson, M.P., Scott, W.G. The structural basis of ribozyme-catalyzed RNA assembly. Science 2007, 315, 1549–50.
65. Giambaşu, G.M., Lee, T.-S.L., Sosa, C.P., Robertson, M.P., Scott, W.G., York, D.M. Identification of dynamical hinge points of the L1 ligase molecular switch. RNA 2010, 16(4), 769–80.
66. Duarte, C.M., Pyle, A.M. Stepping through an RNA structure: A novel approach to conformational analysis. J. Mol. Biol. 1998, 284(5), 1465–78, http://dx.doi.org/10.1006/jmbi.1998.2233.
67. Wadley, L.M., Keating, K.S., Duarte, C.M., Pyle, A.M. Evaluating and learning from RNA pseudotorsional space: Quantitative validation of a reduced representation for RNA structure. J. Mol. Biol. 2007, 372(4), 942–57, http://dx.doi.org/10.1016/j.jmb.2007.06.058.
68. Curtis, E.A., Bartel, D.P. The hammerhead cleavage reaction in monovalent cations. RNA 2001, 7, 546–52.
69. Murray, J.B., Seyhan, A.A., Walter, N.G., Burke, J.M., Scott, W.G. The hammerhead, hairpin and vs ribozymes are catalytically proficient in monovalent cations alone. Chem. Biol. 1998, 5, 587–95.
70. O'Rear, J.L., Wang, S., Feig, A.L., Beigelman, L., Uhlenbeck, O.C., Herschlag, D. Comparison of the hammerhead cleavage reactions stimulated by monovalent and divalent cations. RNA 2001, 7. 537–45.
71. Davis, J.H., Foster, T.R., Tonelli, M., Butcher, S.E. Role of metal ions in the tetraloop-receptor complex as analyzed by NMR. RNA 2007, 13(1), 76–86. http://dx.doi.org/10.1261/rna.268307
72. Mayaan, E., Moser, A., Mackerell, A.D. Jr., York, D.M. CHARMM force field parameters for simulation of reactive intermediates in native and thio-substituted ribozymes. J. Comput. Chem. 2007, 28, 495–507.
73. Przybilski, R., Hammann, C. The tolerance to exchanges of the Watson Crick base pair in the hammerhead ribozyme core is determined by surrounding elements. RNA 2007, 13, 1625–30.
74. Burgin, A.B., Jr., Gonzalez, C., Matulic-Adamic, J., Karpeisky, A.M., Usman, N., McSwiggen, J.A., Beigelman, L. Chemically modified hammerhead ribozymes with improved catalytic rates. Biochemistry 1996, 35, 14090–7.
75. Soukup, G.A., Breaker, R.R. Relationship between internucleotide linkage geometry and the stability of RNA. RNA 1999, 5, 1308–25.

76. Baidya, N., Uhlenbeck, O.C. A kinetic and thermodynamic analysis of cleavage site mutations in the hammerhead ribozyme. Biochemistry 1997, 36, 1108–14.
77. Ruffner, D.E., Stormo, G.D., Uhlenbeck, O.C. Sequence requirements of the hammerhead RNA self-cleavage reaction. Biochemistry 1990, 29, 10695–712.
78. Han, J., Burke, J.M. Model for general acid-base catalysis by the hammerhead ribozyme: pH-activity relationships of G8 and G12 variants at the putative active site. Biochemistry 2005, 44, 7864–70.
79. Nelson, J.A., Uhlenbeck, O.C. Minimal and extended hammerheads utilize a similar dynamic reaction mechanism for catalysis. RNA 2008, 14(1), 43–54, http://dx.doi.org/10.1261/rna.717908.
80. Steitz, T.A. DNA- and RNA-dependent DNA polymerases. Curr. Opin. Struct. Biol. 1993, 3, 31–8.
81. Steitz, T.A., Steitz, J.A. A general two-metal-ion mechanism for catalytic RNA. Proc. Natl. Acad. Sci. U.S.A. 1993, 90, 6498–502.
82. Leontis, N.B., Stombaugh, J., Westhof, E. The non-Watson-Crick base pairs and their associated isostericity matrices. Nucleic Acids Res. 2002, 30, 3497–531.
83. Phillips, J.C., Braun, R., Wang, W., Gumbart, J., Tajkhorshid, E., Villa, E., Chipot, C., Skeel, R.D., Kaleé, L., Schulten, K. Scalable molecular dynamics with NAMD. J. Comput. Chem. 2005, 26, 1781–802.
84. Cornell, W.D., Cieplak, P., Bayly, C.I., Gould, I.R., Ferguson, D.M., Spellmeyer, D.C., Fox, T., Caldwell, J.W., Kollman, P.A. A second generation force field for the simulation of proteins, nucleic acids and organic molecules. J. Am. Chem. Soc. 1995, 117, 5179–97.
85. Case, D., Darden, T., Cheatham, T. III, Simmerling, C., Wang, J., Duke, R., Luo, R., Crowley, M., Walker, R., Zhang, W., Merz, K., Wang, B., Hayik, S., Roitberg, A., Seabra, G., Kolossváry, I., Wong, K., Paesani, F., Vanicek, J., Wu, X., Brozell, S., Steinbrecher, T., Gohlke, H., Yang, L., Tan, C., Mongan, J., Hornak, V., Cui, G., Mathews, D., Seetin, M., Sagui, C., Babin, V., Kollman, P. AMBER 10, University of California, San Francisco, 2002.
86. Case, D.A., Cheatham, T.E.III, Darden, T., Gohlke, H., Luo, R., Merz, K.M., Onufriev, A., Simmerling, C., Wang, B., Woods, R.J. The AMBER biomolecular simulation programs. J. Comput. Chem. 2005, 26, 1668–88.
87. Pearlman, D.A., Case, D.A., Caldwell, J.W., Ross, W.R., Cheatham, T., III, DeBolt, S., Ferguson, D., Seibel, G., Kollman, P. AMBER, a package of computer programs for applying molecular mechanics, normal mode analysis, molecular dynamics and free energy calculations to simulate the structure and energetic properties of molecules. Comput. Phys. Commun. 1995, 91, 1–41.
88. Jorgensen, W.L., Chandrasekhar, J., Madura, J.D., Impey, R.W., Klein, M.L. Comparison of simple potential functions for simulating liquid water. J. Chem. Phys. 1983, 79, 926–35.
89. Feller, S., Zhang, Y., Pastor, R., Brooks, B. Constant pressure molecular dynamics simulation: The Langevin piston method. J. Chem. Phys. 1995, 103, 4613–21.
90. Martyna, G.J., Tobias, D.J., Klein, M.L. Constant pressure molecular dynamics algorithms. J. Chem. Phys. 1994, 101, 4177–89.
91. Essmann, U., Perera, L., Berkowitz, M.L., Darden, T., Hsing, L., Pedersen, L.G. A smooth particle mesh Ewald method. J. Chem. Phys. 1995, 103(19), 8577–93.
92. Sagui, C., Darden, T.A. Molecular dynamics simulations of biomolecules: Long-range electrostatic effects. Annu. Rev. Biophys. Biomol. Struct. 1999, 28, 155–79.
93. Allen, M., Tildesley, D. Computer Simulation of Liquids, Oxford University Press, Oxford, 1987.
94. Ryckaert, J.P., Ciccotti, G., Berendsen, H.J.C. Numerical integration of the Cartesian equations of motion of a system with constraints: Molecular dynamics of n-Alkanes. J. Comput. Phys. 1977, 23, 327–41.
95. Nam, K., Cui, Q., Gao, J., York, D.M. Specific reaction parametrization of the AM1/d Hamiltonian for phosphoryl transfer reactions: H, O, and P atoms. J. Chem. Theory Comput. 2007, 3, 486–504.
96. Hutter, M.C., Reimers, J.R., Hush, N.S. Modeling the bacterial photosynthetic reaction center. 1. Magnesium parameters for the semiempirical AM1 method developed using a genetic algorithm. J. Phys. Chem. B 1998, 102, 8080–90.
97. Brooks, B.R., Bruccoleri, R.E., Olafson, B.D., States, D.J., Swaminathan, S., Karplus, M. CHARMM: A program for macromolecular energy minimization and dynamics calculations. J. Comput. Chem. 1983, 4, 187–217.

98. Foloppe, N., MacKerell, A.D., Jr. All-atom empirical force field for nucleic acids: I. Parameter optimization based on small molecule and condensed phase macromolecular target data. J. Comput. Chem. 2000, 21, 86–104.
99. MacKerell, ,A.D. Jr., Banavali, N.K. All-atom empirical force field for nucleic acids: II. Application to molecular dynamics simulations of DNA and RNA in solution. J. Comput. Chem. 2000, 21, 105–20.
100. Gao, J., Amara, P., Alhambra, C., Field, M.J. A generalized hybrid orbital (GHO) method for the treatment of boundary atoms in combined QM/MM calculations. J. Phys. Chem. A 1998, 102, 4714–21.
101. Nam, K., Gao, J., York, D.M. An efficient linear-scaling Ewald method for long-range electrostatic interactions in combined QM/MM calculations. J. Chem. Theory Comput. 2005, 1(1), 23–13.